








Design and Evaluation of C-Band Microstrip Antenna Array for Portable Ground Surveillance Radar

Ian Josef Matheus Edward ^{1*}, Tommi Hariyadi ², Wervyan Shalannanda ¹,
Endon Bharata ¹, Donny Danudirdjo ¹, Yosi A. Hidayat ¹, Dharma Favitri Hariyanto ³,
Alvin Mustafa ³, Kusmadi ⁴, Sapto Adi Nugroho ¹, Nerissa Arviana Ridwan ⁴

¹ School of Electrical Engineering and Informatics, Institut Teknologi Bandung, Bandung 40132, Jawa Barat, Indonesia.

² Korea Advanced Institute of Science and Technology (KAIST), School of Electrical Engineering, Daejeon, 34141, South Korea.

³ PT Kreasi Rekayasa Indonesia (KIREI), Bandung, Indonesia.

⁴ Department of Industrial Engineering, Faculty of Engineering, Universitas Sangga Buana, Bandung, Indonesia.

Abstract

This study aims to design, simulate, fabricate, and evaluate a high-gain C-band microstrip antenna array with a corrugation plate for Portable Ground Surveillance Radar (PGSR) applications, addressing the need for compact, high-performance antennas in border security operations. The proposed design targets a minimum gain of 20 dBi, a horizontal beamwidth of $\leq 2.8^\circ$, a vertical beamwidth of $\leq 7.5^\circ$, horizontal polarization, and compact physical dimensions for field portability. The methodology involved electromagnetic simulations to optimize the slit-patch array geometry, fabrication using Rogers RO-4350B substrate for its stable dielectric properties, and performance validation in an anechoic chamber using a vector network analyzer. The fabricated prototype achieved strong agreement with simulations in key metrics: realized gain exceeded 20 dBi, return loss reached -27.35 dB, and SWR was approximately 1.2, confirming effective impedance matching. The corrugation plate enhanced impedance matching, improved transmission efficiency (S21), and reduced reverse isolation (S12), while S22 remained stable. Despite these strengths, the measurement beamwidths, especially vertical beamwidth ($\sim 30^\circ$), exceeded both simulation and target values, highlighting fabrication precision and alignment as areas for improvement. The novelty of this work lies in integrating a corrugation plate to improve impedance matching and the correlation between simulation and measurement, offering a practical, tuneable enhancement to microstrip antenna arrays for PGSR and similar radar systems.

Keywords:

C-band Antenna;
Microstrip Patch Antenna Array;
FMCW Radar.

Article History:

Received:	02	July	2025
Revised:	17	September	2025
Accepted:	06	October	2025
Published:	01	December	2025

1- Introduction

As a nation composed of thousands of islands, Indonesia faces unique security challenges. Its vast maritime and land borders, combined with strategic geographic placement and rich natural resources, create a need for effective surveillance systems to ensure the safety and integrity of its territories [1, 2]. In recent years, portable ground surveillance radar systems have become crucial tools for quickly identifying potential threats. These systems are vital for detecting unauthorized vehicle movements, spotting unmanned aerial vehicles (UAVs), and monitoring individuals crossing borders illegally or covertly [3].

* **CONTACT:** ian@itb.ac.id

DOI: <http://dx.doi.org/10.28991/ESJ-2025-09-06-015>

© 2025 by the authors. Licensee ESJ, Italy. This is an open access article under the terms and conditions of the Creative Commons Attribution (CC-BY) license (<https://creativecommons.org/licenses/by/4.0/>).

Portable Ground Surveillance Radar (PGSR) systems provide a range of strategic benefits that make them valuable for various missions. Their compact design and lightweight nature make them easy to transport and set up, which is crucial in situations where time and stealth are essential. These radars are often based on Frequency Modulated Continuous Wave (FMCW) technology, which is known for its low power emissions. This feature minimizes the probability of detection by adversaries and increasing the overall stealth of operations [4]. Recent primers and application surveys further underline FMCW's relevance to small-UAV detection and fieldable platforms, including the role of full-wave EM/CAD in end-to-end radar/antenna co-design [5, 6].

Within PGSR, microstrip arrays remain attractive for their planar profile, manufacturability, and integrability with RF front ends. Over the last few years, related C-band and surveillance-adjacent work has emphasized high gain, pattern control, and array-level coupling/isolation: C-band feed/array solutions and C-band weather-radar arrays have been demonstrated, including designs on Rogers 4350/RO4350B similar to ours; other efforts explore series-fed or corporate-fed arrays targeting narrow HPBW and low sidelobes [7-10]. In parallel, reviews and techniques literature, whose topics are highly connected to our beamwidth and isolation goals, highlight pattern shaping (beamforming, flat-top/HPBW control), isolation and mutual-coupling mitigation (e.g., parasitics, EBG/superstrates, defected grounds), and their trade-offs for array performance [11-14].

Our previous conference papers presented a horizontally polarized, C-band, single-layer corporate-fed slit-patch array that met key targets (frequency, gain, polarization, physical size) but did not meet the beamwidth limits required for PGSR situational awareness [15, 16]. Similar challenges appear across recent array reports: while gain/return-loss targets are routinely achieved, half-power beamwidth (HPBW) and sidelobe control can be sensitive to inter-element coupling, finite-aperture/edge diffraction, feeding non-idealities, and assembly tolerances, particularly when compact panels push element spacing near mutual-coupling regimes. Several prior studies document these sensitivities and propose remedies (e.g., parasitic directors/superstrates for pattern shaping or coupling suppression, non-uniform corporate feeds, and series-fed layouts), underscoring the need for combined electromagnetic and mechanical co-optimization [17-19].

Gap and approach: Against this background, the specific gap we address is *beamwidth compliance in a compact, horizontally polarized C-band microstrip array for PGSR* without sacrificing gain or portability. Building on our slit-patch concept, we introduce and experimentally study a tuning element (a “corrugation plate”) intended to (a) improve impedance matching and forward transmission (S₂₁), (b) enhance reverse isolation (S₁₂), and (c) narrow the discrepancy between simulated and measured responses. Compared with recent C-band/array implementations, which emphasize gain and bandwidth or broad-beam coverage, our focus is on *HPBW control and isolation in a compact PGSR-class array*, validated through side-by-side simulation-measurement comparisons.

Contributions: (1) A compact C-band slit-patch array design for PGSR with documented trade-offs versus alternative polarization and pattern-control techniques; (2) an experimentally validated tuning plate that measurably improves matching (S₁₁/SWR), transmission (S₂₁), and reverse isolation (S₁₂); (3) an extended analysis explaining residual beamwidth deviations due to coupling/edge effects and fabrication/alignment tolerances, and mapping mitigation paths consistent with recent isolation/beam-shaping literature [12, 14].

2- Literature Review

In recent years, ground surveillance radars have made remarkable progress. This evolution has been largely driven by the increasing need for national security, effective border protection, and military operations. For instance, Davis (2015) provides a detailed look at how battlefield surveillance radars have changed over time, emphasizing their essential role in contemporary military conflicts and the importance of situational awareness [1]. At the same time, Heinbach et al. (2014) shed light on the rise of Low Probability of Intercept (LPI) radars. These radars have become significant because they are harder for enemies to detect, which gives military operations a strategic edge by enhancing covert capabilities during surveillance missions [2]. FMCW architectures have since become the choice for portable systems due to their simultaneous range-Doppler capability and inherent low-intercept emissions; recent primers focused on UAV detection also emphasize the role of EM-CAD and measurement discipline in translating simulation to field performance [3, 5, 6].

Microstrip antenna technologies, especially patch arrays, have become quite popular in modern radar systems. Their compact size, ease of integration, and flexibility in manufacturing make them a great choice for a wide range of applications. For instance, Wang et al. (2008) presented an interesting design for a single-layer wideband U-slot microstrip patch antenna array. This design showcases impressive gain and a broad operational bandwidth, which can be particularly useful for surveillance radar applications [20]. In a similar vein, Huque et al. [21] explored microstrip array antennas that are specifically optimized for X-band radar systems. They highlighted several key design parameters, such as gain and beamwidth, which are crucial for ensuring effective radar performance. Other recent studies on C-band report practical feed and array implementations, including RO4350-class substrates, demonstrating that gain and matching targets are routinely achievable in compact panels [7-9]. For radar-adjacent applications, low-sidelobe and narrow-beam array designs continue to evolve; recent demonstrations in obstacle-detection systems show how feed

topology and amplitude tapering suppress sidelobes while preserving bandwidth and aperture efficiency [10]. Reviews of array beamforming techniques further codify pattern-control strategies (digital/hybrid/analog) that inform HPBW and sidelobe trade-offs when physical aperture and element spacing are constrained [11].

A persistent theme in compact arrays is isolation and coupling control, because inter-element interactions, finite-aperture/edge diffraction, and feed non-idealities can broaden the main lobe and elevate sidelobes. Recent studies reduce coupling via frequency-selective surfaces (FSS), EBG/superstrates, and defected ground structures (DGS), reporting measurable improvements in return loss, HPBW, and S-parameters in both simulations and prototypes [22-24]. Classic techniques (e.g., erected walls/shorting pins) remain relevant for compact panels where element spacing is pushed toward mutual-coupling regimes [25]. In parallel, new works at mm-wave demonstrate array-pattern engineering (series / corporate feeds, parasitic/superstrate loading, non-uniform amplitude) that are directly translatable to C-band when scaled, reinforcing the link between feed network choices, isolation treatments, and beamwidth outcomes [9, 10, 26].

Against this backdrop, our prior designs validated a horizontally polarized, single-layer, corporate-fed slit-patch array that met frequency, gain, and size requirements, but struggled to satisfy HPBW limits for PGSR [15, 16]. The literature above suggests two complementary options for improvement: (1) tuning the impedance and isolation to tighten the match and reduce reverse/port coupling (e.g., via engineered plates/superstrates or DGS/EBG/FSS insertions), and (2) shaping the pattern shaping through feed equalization and controlled parasitics. The present work contributes along the first option by introducing a tuning (“corrugation”) plate and experimentally showing improved S11/SWR, higher S21, and lower S12 with a stronger simulation-measurement agreement, while documenting residual HPBW gaps attributable to coupling/edge effects and assembly tolerances, phenomena reported in recent array literature [10, 22-24].

3- Antenna Design Requirements and Methodology

3-1-Antenna Specifications

The development of antennas for Portable Ground Surveillance Radar (PGSR) systems requires adherence to rigorous operational criteria crucial for optimal field performance. The antenna must operate effectively within the C-band frequency range and achieve a minimum gain of 20 dBi to ensure adequate detection capability at extended ranges. Furthermore, precise control of beamwidth is imperative; hence, the horizontal beamwidth must not exceed 2.8 degrees, while the vertical beamwidth should be maintained within 7.5 degrees. These specifications are vital for ensuring directional accuracy and enhancing target discrimination. Additionally, the antenna must incorporate horizontal polarization to align with the operational requirements of the system. Importantly, the entire antenna assembly must conform to stringent physical dimensions, specifically limited to less than 100 cm × 42.9 cm × 18.2 cm. This compact design is essential for facilitating ease of transport and enabling rapid deployment during tactical operations [15, 16].

3-2-Antenna Design Approach

To meet the rigorous specifications outlined, this design employs a microstrip patch antenna array, selected for its compact profile, ease of manufacturing, and established effectiveness in microwave radar applications. The configuration of the array is based on a single-layer design that incorporates a corporate feed network. This arrangement facilitates uniform amplitude and phase distribution across the various antenna elements, thereby ensuring consistent performance across the entire array [20]. A critical element of this design was the achievement of horizontal polarization without compromising the antenna’s efficiency or increasing its complexity. To fulfill this requirement, a strategically placed slit was introduced in each antenna patch element. This alteration was essential for directing the current flow horizontally, thus achieving the desired polarization while mitigating unwanted electromagnetic coupling between adjacent elements. Effective reduction of these couplings is crucial, as excessive interaction between patches can impair the performance of individual elements and diminish the overall effectiveness of the array [15, 16].

The design of the antenna incorporated Rogers RO-4350B substrate material, which was chosen for its advantageous electrical properties, including a dielectric constant (ϵ_r) of 3.66 and a low dissipation factor ($\tan \delta$) of 0.0037. These characteristics not only ensure robust mechanical stability but also facilitate compatibility with high-precision fabrication techniques [16]. Such properties are vital for maintaining the consistency of antenna performance, particularly under diverse environmental conditions and operational stresses that may arise during real-world deployments. Through a meticulous design process, the antenna demonstrated its ability to meet critical specifications in both simulation studies and initial practical applications. Despite these achievements, challenges persisted in achieving precise control over horizontal and vertical beamwidth, highlighting the need for ongoing refinement. Future efforts will focus on iterative enhancements supported by additional measurements and optimization processes to address these challenges effectively.

3-3- Theoretical Basis and Design Rationale

3-3-1- Polarization Control via Slit-Loaded Patch

A square/rectangular microstrip patch supports two orthogonal dominant modes (TM_{10} and TM_{01}), with surface currents flowing primarily along the patch's principal axes. Introducing a narrow slit near a patch edge disturbs the local current path and adds a small capacitive loading that detunes one orthogonal mode while favoring the other. In our layout, the slit placement and length are selected to reinforce the mode whose surface current runs horizontally, thereby yielding the required horizontal polarization while keeping the feed network compact (single-layer, corporate feed). From an equivalent-circuit standpoint, the patch can be viewed as a parallel RLC resonator; the slit adds a series capacitance C_{slot} that slightly shortens the effective electrical length along one axis, shifting the modal balance and reducing cross polarization. Qualitative field plots from simulation (Section 4.1) corroborate this behavior by showing horizontally oriented \mathbf{J}_s on the patch surface [11, 15, 16, 20].

3-3-2- Array Factor, Beamwidth Targets, and Aperture Limits

The far-field of a planar array factorizes into the element pattern and the array factor (AF). For a uniformly excited $M \times N$ rectangular array with inter-element spacings d_x and d_y , broadside steering, and negligible mutual coupling, the AF lobes are set by aperture size $D_x \approx N d_x$ and $D_y \approx M d_y$. A practical rule-of-thumb for the half-power beamwidth (HPBW) of a uniformly illuminated 1-D aperture is

$$HPBW \text{ (deg)} \approx 50.7 \frac{\lambda}{D} \quad (1)$$

with a first sidelobe around -13.2 dB for uniform taper. At 5.6 GHz, $\lambda \approx 53.6$ mm. Meeting the horizontal HPBW requirement of 2.8 degrees implies an effective horizontal aperture of

$$D_x \approx \frac{50.7\lambda}{2.8^\circ} \approx \frac{50.7 \times 53.6 \text{ mm}}{2.8} \approx 970 \text{ mm} \quad (2)$$

while the vertical HPBW target 7.5 degrees implies:

$$D_y \approx \frac{50.7\lambda}{7.5^\circ} \approx 362 \text{ mm}. \quad (3)$$

These back-of-the-envelope bounds explain a central trade-off in our compact C-band panel: with a front dimension of roughly 380 mm \times 162 mm for a 4×12 array, the realized HPBWs in simulation ($\approx 7.1^\circ, 17.4^\circ$) are consistent with the physical aperture limits and the chosen uniform excitation. Element spacing is also constrained by grating-lobe avoidance ($d \leq \lambda/2$ for broadside), further restricting aperture growth in a compact panel [10, 11, 15, 16, 22-24].

3-3-3- Impedance Matching and Isolation: Role of the Corrugation Plate

The "corrugation plate" (a thin metallic/superstrate-like plate placed near the aperture modifies the near-field boundary conditions and acts as a reactive loading structure. In an equivalent-admittance picture, the input admittance at the feed is $Y_{in} = G + jB$, which is complemented by a plate-induced susceptance jB_p , appropriately choosing plate dimensions/height can drive $B + B_p \rightarrow 0$, thereby improving match and lowering

$$|\Gamma| = \left| \frac{Z_{in} - Z_0}{Z_{in} + Z_0} \right| \quad (4)$$

(observed as reduced $|S_{11}|$ and SWR in Section 5.3). The plate also redistributes fringing fields at the array edges, which weakens unwanted coupling paths and improves reverse isolation (S_{12}), while preserving S_{22} stability. Experimentally we observe higher S_{21} (better forward transmission) and deeper S_{11} notches with the plate installed. This is consistent with a parasitic/tuning element that performs mild impedance transformation and edge-field shielding [15, 16, 22-24].

3-3-4- Sensitivity Considerations (Substrate, Geometry, Feed, and Plate)

Substrate & resonance: Small dielectric changes shift the resonant frequency approximately as $\frac{\Delta f}{f} \approx -\frac{1}{2} \Delta \epsilon_{\text{eff}}$.

Thus, a higher ϵ_r lowers f_0 and modifies input reactance/match bandwidth [16, 20].

Patch geometry: length/width tolerances change frequency and pattern according to $\Delta f/f \approx -\Delta L/L$. Over-etch or under-etch of the patch can move the S_{11} dip and alter cross-polarization, consistent with the observed simulation-measurement offsets [15, 16, 20].

Slit parameters (length/offset/width): a longer slit strengthens the desired horizontal mode, but adds capacitive loading that shifts f_0 ; over-extension or lateral offset errors can unbalance modal fields and raise cross-polarization or perturb S_{11} [20].

Corrugation plate height h_p : The plate contributes a susceptance $B_p(h_p)$. There is typically an optimum h_p where $B + B_p \rightarrow 0$, yielding the deepest S_{11} notch and lowest SWR, with S_{21} peaking near that region. Deviating from this height detunes the match and can waken isolation gains (higher S_{12}), in line with Section 5.3 trends [22-24].

[10, 16, 22-24] Inter-element spacing & aperture: with broadside steering, $d \leq \lambda/2$ avoids grating lobes. The compact panel limits the effective aperture D , so $\text{HPBW} \propto \lambda/D$ predicts broader beams; small spacing changes ($\approx \pm 5\%$) shift HPBW/sidelobes and coupling. This explains the persistent elevation-beamwidth gap in a 380 x 162 mm panel [10, 11, 15, 16].

Corporate-feed errors: Amplitude errors ($\approx \pm 5\%$) and phase errors ($\approx \pm 5^\circ$) elevate sidelobes and can tilt the main beam, affecting HPBW and measured cuts, careful layout, and calibration reduce these effects [11, 22].

Practical implication: These sensitivities explain the good agreement in matching/transmission/isolation when the plate is used (Section 5), and why the HPBW gap is primarily an aperture/coupling issue rather than a pure matching problem (Section 4-6).

3-3-5- Trade-offs in Polarization-Control Techniques

We adopted a slit-loaded, single-feed patch to enforce horizontal polarization while keeping a single-layer, corporate-fed layout. This choice keeps the profile low, avoids multilayer vias/hybrids, and integrates cleanly with the array feed. The main trade-offs are: (1) narrower tuning margin, as the slit perturbs the current path and adds a small capacitive loading, so etch and placement tolerances directly affect polarization purity and match; (2) potential cross-polarization rise if the slit is mispositioned or over-/under-length; and (3) modest sensitivity of S_{11} to slit length/offset due to the added susceptance (see 3.3.3) [11, 15, 16, 20].

Alternative methods and their implications for a compact PGSR panel include:

- Dual-feed orthogonal modes: excellent control of polarization/axial ratio and robust tuning, but adds feed complexity, insertion loss, phase-balance tolerance, and broad area/weight, which are undesirable in a single-layer, fieldable panel [11, 20].
- Probe-feed rotation/tilted feed: simple mechanically but increases profile and can introduce spurious radiation and pattern asymmetry; routing becomes congested in larger 4x12 layouts.
- Sequential/rotation subarrays: good axial ratio and sidelobe control via progressive phase, but requires subarray phasing networks and extra footprint, which comes with feed complexity and loss [11].
- Parasitics/superstrates/EBG/DGS treatments: can improve isolation and shape patterns, but add fabrication steps, thickness/weight, and risk bandwidth narrowing or detuning if not co-optimized [22-24].

Given PGSR constraints (portability, single-layer build, corporate feed), the slit-loaded patch offered the best complexity-performance balance while preserving a path to future add-ons (e.g., mild amplitude tapering of edge treatments) for HPBW/sidelobe improvement [10, 11, 15, 16, 20, 23, 24].

3-4- Methodological Workflow

The development flow for the PGSR C-band array is summarized in Figure 1. We begin by consolidating requirements and constraints as mentioned in subsection 3.1. These drive the element design (slit-loaded patch for horizontal polarization) and a single-layer corporate feed that equalizes amplitude/phase across the aperture. We then run full-wave simulations from the element to the 4x12 array to evaluate return loss (S_{11}) forward transmission (S_{21}), HPBW in azimuth/elevation, and coupling/sidelobe behavior. If the beamwidth targets are not achieved, we iterate on inter-element spacing, light amplitude taper, slit length/offset, and corrugation-plate height. Once the electrical design complies with the requirements, we proceed to fabrication on RO4350b and panel assembly, followed by anechoic-chamber setup (VNA connection, alignment, and calibration). In this prototype cycle, the measurement campaign focuses on S-parameters (S_{11} , S_{21} , S_{12} , S_{22}) and SWR, which are used in the extended analysis to compare “with-plate” and “without-plate” configurations and to interpret the tuning/isolation effects. Finally, we consolidate conclusions and define next-iteration actions (pattern-control options, plate optimization, modeling, and measurement refinements).

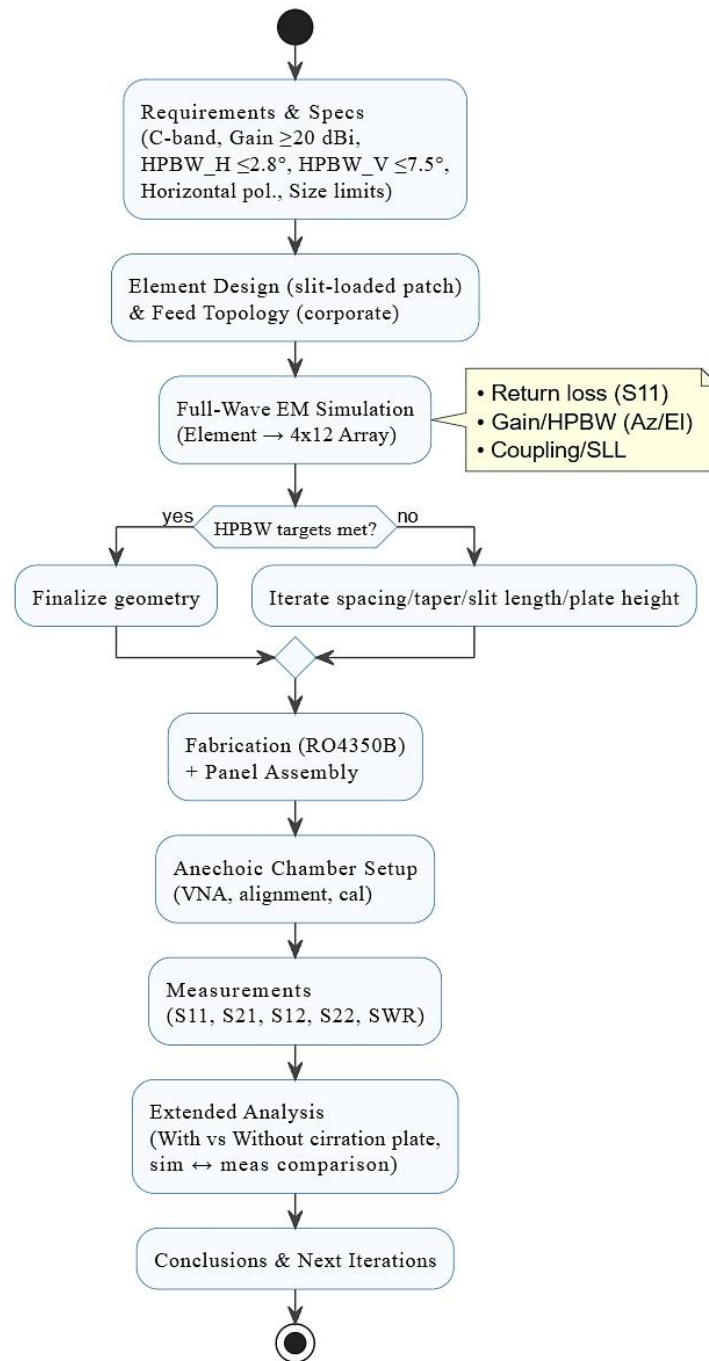


Figure 1. Design-fabrication-measurement workflow

4- Antenna Simulation

4-1- Single-Element Antenna Simulation

The development of the antenna commenced with a focused effort on simulating a single-element design. This initial phase aimed to establish baseline characteristics and verify core performance parameters prior to the expansion into a more comprehensive array configuration. Conducting this preliminary simulation was crucial for ensuring that the fundamental properties of the antenna—such as gain, polarization, and operational frequency—aligned with the specified design objectives [15]. The results gathered from the single-element simulation revealed that the antenna achieved an approximate gain of 5.5 dBi at the targeted operational frequency of 5.6 GHz, which falls within the C-band spectrum. Furthermore, the simulations provided clear evidence that the antenna achieved the anticipated horizontal polarization. This was substantiated through an analysis of the current distribution patterns observed on the surfaces of the patch. This foundational phase of the project yielded critical insights, particularly regarding the behavior of individual antenna elements. These insights proved invaluable for guiding necessary modifications as the design progressed toward a more

intricate antenna array. Additionally, this early simulation stage facilitated the identification and rectification of significant design flaws, thus enhancing the overall efficacy of the development process.

4-2- 4×12 Array Antenna Simulation

This study builds upon the validated design of a single-element antenna, paving the way for extensive simulations of a 4×12 antenna array that aligns with the operational specifications required for Portable Ground Surveillance Radars (PGSR). The expansion to this larger array configuration was instrumental in achieving the necessary higher gain, narrower beamwidth, and improved radar detection capabilities essential for the application's success. The simulation results for the array antenna proved to be promising. Notably, a realized gain of approximately 21.66 dBi was attained, which significantly exceeds the minimum specification threshold of 20 dBi. Furthermore, the antenna exhibited robust performance at the operational frequency, evidenced by a return loss level of below -30 dB at 5.6 GHz. This performance metric reflects efficient power transmission and minimal signal reflections, both critical factors that ensure optimal radar functionality and mitigate potential interference issues [15]. The corresponding simulated radiation patterns are shown in Figures 2 and 3.

Recent simulations have unveiled notable challenges in adhering to the stringent beamwidth specifications required for optimal performance. As anticipated from the aperture bound in Section 3.3.2, the simulated HPBW reflects the physical-size constraint of the compact panel. The results indicated that the simulated horizontal beamwidth was approximately 7.1 degrees, significantly surpassing the desired target of 2.8 degrees. Likewise, the vertical beamwidth measured approximately 17.4 degrees, more than double the intended target of 7.5 degrees [15, 16]. These considerable deviations underscore the inherent challenges in precisely controlling directional beam patterns within larger antenna arrays. The discrepancies observed in beamwidth values suggest that further optimization of the design is essential. Potential strategies for enhancement may include adjustments to inter-element spacing or refinements in the design of individual antenna elements. These simulation results highlight the critical need for ongoing iterative improvements and further detailed measurements, specifically aimed at narrowing the beamwidths to satisfy the practical requirements of surveillance radar applications.

The observed discrepancies in beamwidth values indicated a need for further design optimization. This could involve adjustments to the inter-element spacing or refinement of individual antenna elements. As a result, the simulation findings underscored the importance of ongoing iterative improvements and the necessity for more detailed measurements. These efforts are specifically aimed at narrowing the beamwidths in order to align with the practical requirements of surveillance radar systems.

The simulated HPBW ($\approx 7.1^\circ$ azimuth; $\approx 17.4^\circ$ elevation) did not meet the target values (2.8° ; 7.5°). As discussed in the aperture bound (Section 3.3.2), the compact front dimension of the 4×12 panel ($\approx 380 \text{ mm} \times 162 \text{ mm}$) at 5.6 GHz inherently limits the achievable HPBW, even with uniform corporate feeding. Additional broadening from mutual coupling and finite-aperture/edge effects (Section 3.3.4) further explains the elevation deviation [10, 11, 15, 16]. Despite observing this gap in simulation, we proceeded to fabrication for two reasons: (1) project schedule and funding deliverables required a hardware prototype, and (2) we sought to empirically validate the matching / transmission / isolation behavior and the impact of the corrugation plate under measurement (Sections 5-6).

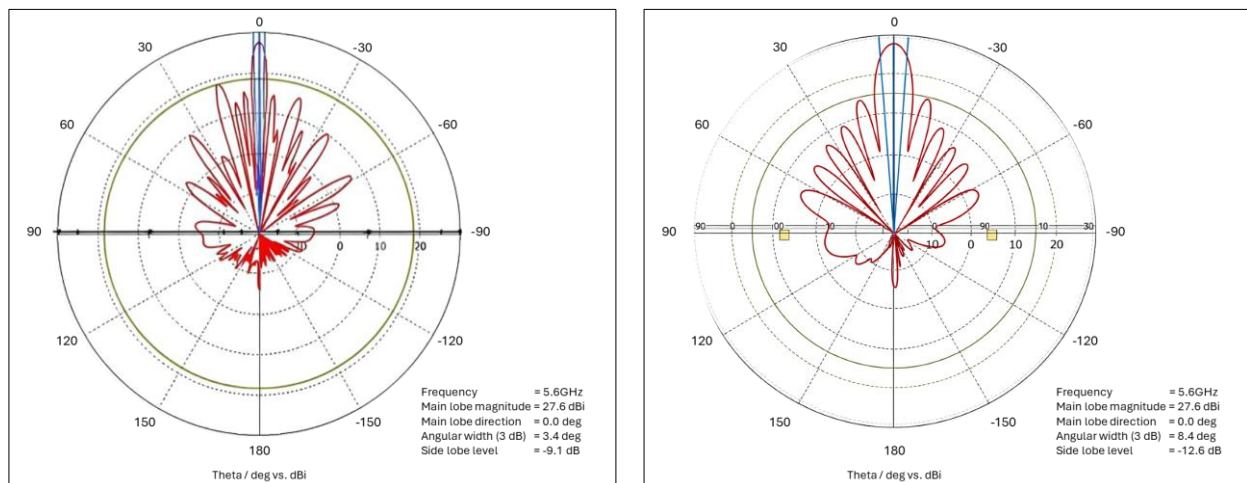


Figure 2. Radiation Pattern of the Antenna Array-1

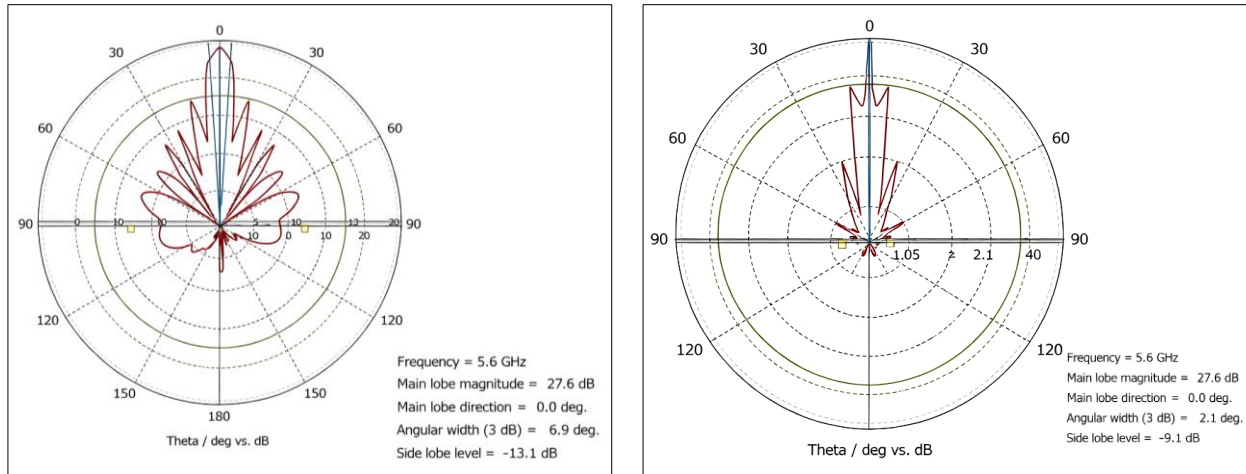


Figure 3. Radiation Pattern of the Antenna Array-2

5- Antenna Implementation and Measurement

5-1-Antenna Fabrication

Upon the completion of the simulations, the antenna design was fabricated to assess its performance in real-world conditions. For the manufacturing of the antenna, we selected Rogers RO-4350B as the substrate material. This choice was driven by its outstanding electrical properties, particularly its stable dielectric constant of 3.66 and a low dissipation factor of 0.0037. Additionally, the mechanical reliability of this material contributes significantly to the consistency of antenna performance, which is critical given the stringent specifications required for radar applications. The fabrication process adhered strictly to the dimensions obtained from the simulation models, ensuring an accurate representation of the design. Each antenna element incorporated a previously optimized slit configuration, which was strategically employed to achieve horizontal polarization. This slit design was essential for facilitating effective isolation between elements, thereby minimizing undesirable electromagnetic interactions and ensuring consistent performance across the entire antenna array [15, 16].

5-2-Measurement Methodology

To assess the actual performance of the antenna and identify any deviations from the predicted simulation results, a series of comprehensive experimental measurements were conducted. These tests were carried out within a meticulously controlled anechoic chamber, designed to minimize external electromagnetic interference and ensure the accuracy of the measurements obtained. Key parameters evaluated during the testing process included return loss, realized antenna gain, polarization characteristics, and detailed radiation patterns, with specific attention given to beamwidths in both the azimuth and elevation planes. The testing employed high-precision instruments, particularly a vector network analyzer (VNA), which played a crucial role in accurately capturing the performance metrics of the antenna. The experimental setup was carefully calibrated prior to testing to ensure that the measurements were accurate, reliable, and repeatable. This rigorous approach was essential for conducting a credible evaluation of the antenna's performance, allowing for a thorough comparison with the expected simulation results.

In this prototype cycle, we did not perform a calibrated radiation-pattern/HPBW measurement. This decision was made after confirming the scope and facilities available for the scheduled campaign: (1) the chamber and fixtures were configured for network measurements (S-parameters, SWR), but not equipped as a calibrated near-/far-field a pattern range with reference antennas; (2) the time and budget allocated to this build were prioritized per the PI's request, to validate the matching/transmission/isolation behavior and the corrugation-plate effect; and (3) the array pattern risks (aperture limit, edge/coupling sensitivities) were already visible in simulation and documented in our analysis. Consequently, HPBW is reported for simulation only in this revision, while the measured results are limited to S-parameters and SWR. A full pattern-measurement campaign (azimuth/elevation cuts with alignment jigs and range calibration) is planned for the next build.

5-3-Measurement Results

The measurement results demonstrated a strong correlation with the simulated predictions, with only minor discrepancies arising from practical considerations such as manufacturing variances and subtle environmental influences. Specifically, the return loss measurements taken at the operational frequency of approximately 5.6 GHz yielded a value

of about -27.35 dB. This value, while slightly less favorable than the simulated result of -29.82 dB, remains well within the acceptable limits necessary for effective radar operation [16]. Additionally, the measured antenna gain surpassed the required minimum threshold of 20 dBi, aligning closely with prior simulated forecasts. These findings affirm the practical feasibility of the antenna in ensuring sufficient signal strength for radar detection tasks, thus validating its performance in operational scenarios.

The deeper return-loss notch and lower SWR observed near 5.6 GHz (Figures 4 to 7) indicate that the corrugation plate adds a beneficial reactive component that cancels a portion of the input susceptance, thereby improving the input match (reduced S_{11}) and power transfer. In practical terms, better matching lowers reflected power at the feed and allows more energy to be radiated by the aperture, which is consistent with the measured SWR (1.2-1.3). The concurrent increase in S_{21} (Figure 8) implies that the forward transmission path becomes more efficient when the plate is installed and consistent with a mild impedance transformation and fringing-field control near the panel edges. By contrast, the relative stability of S_{22} across configurations suggests that the output port environment is less sensitive to the plate's presence, which aligns with the observation that the plate primarily impacts the driven face and near-edge fields rather than the entire two-port network.

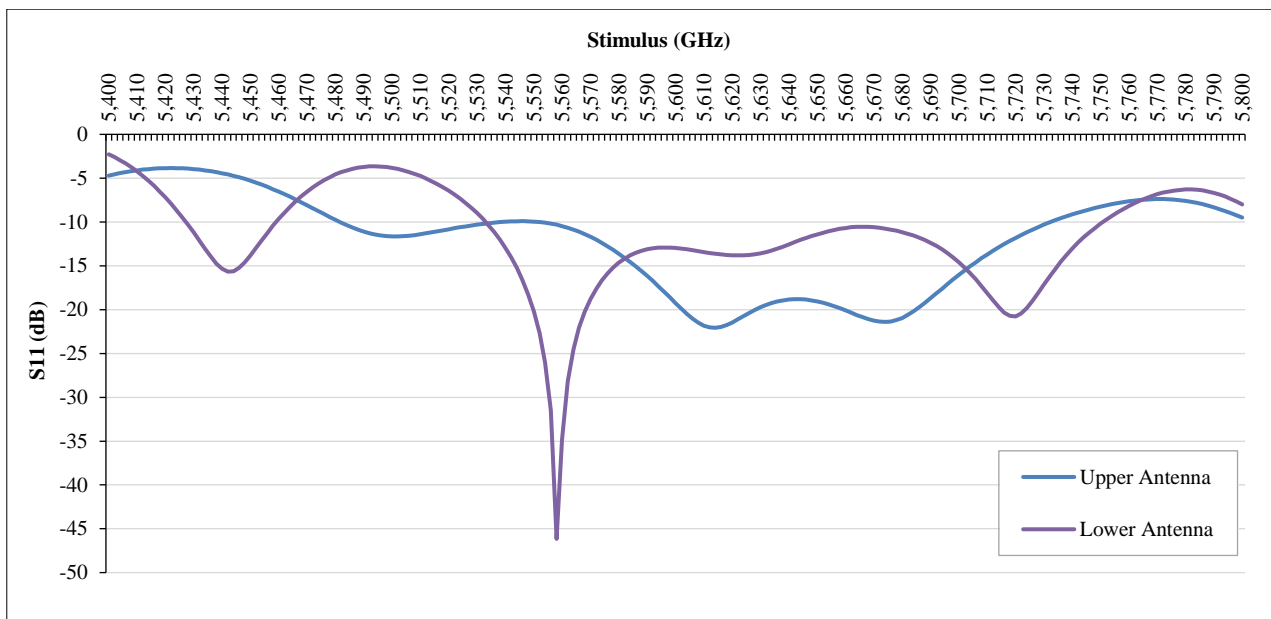


Figure 4. S_{11} measurement with the corrugation plate: The upper antenna is represented in blue, and the lower antenna in purple

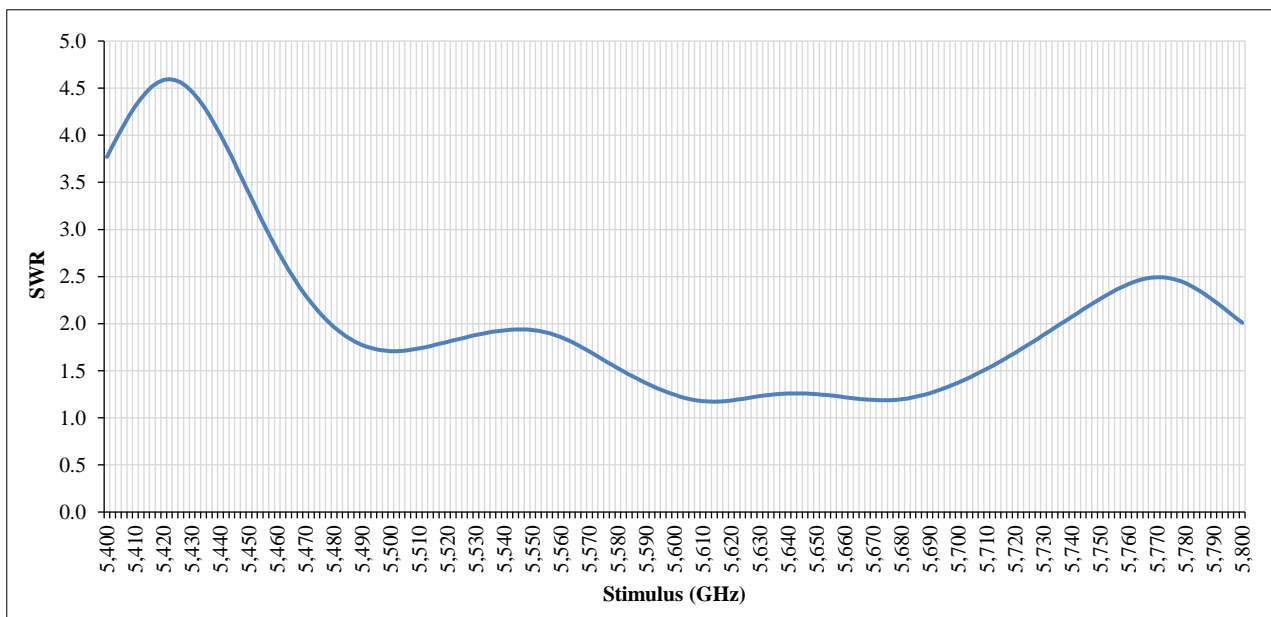


Figure 5. SWR measurement of the upper antenna with the corrugation plate

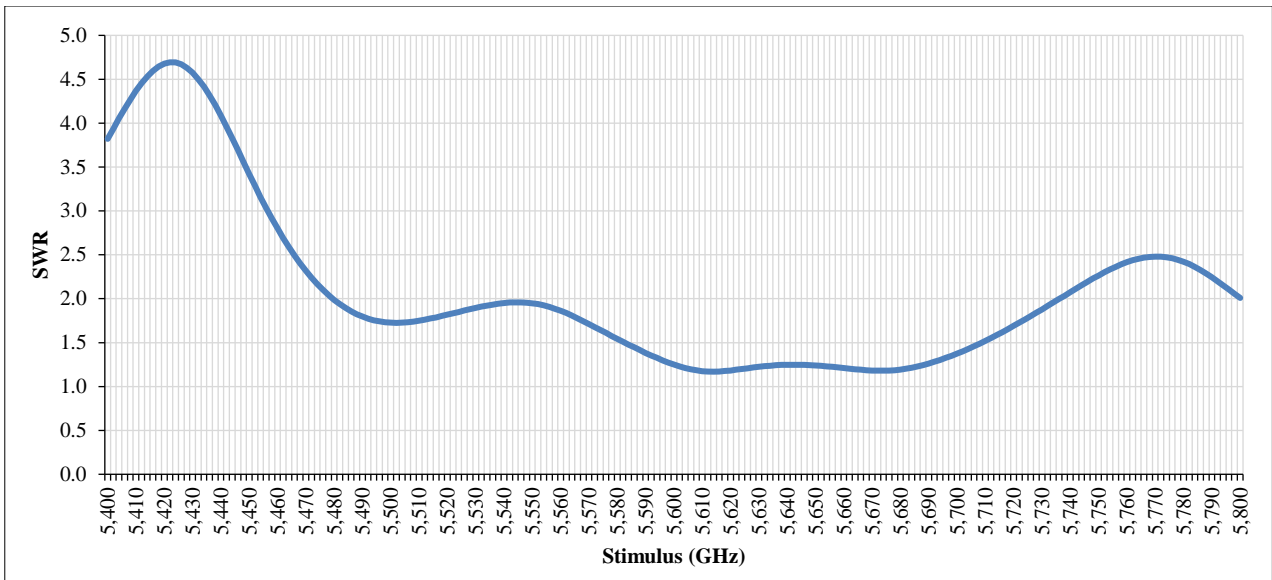


Figure 6. SWR measurement of the upper antenna without the corrugation plate

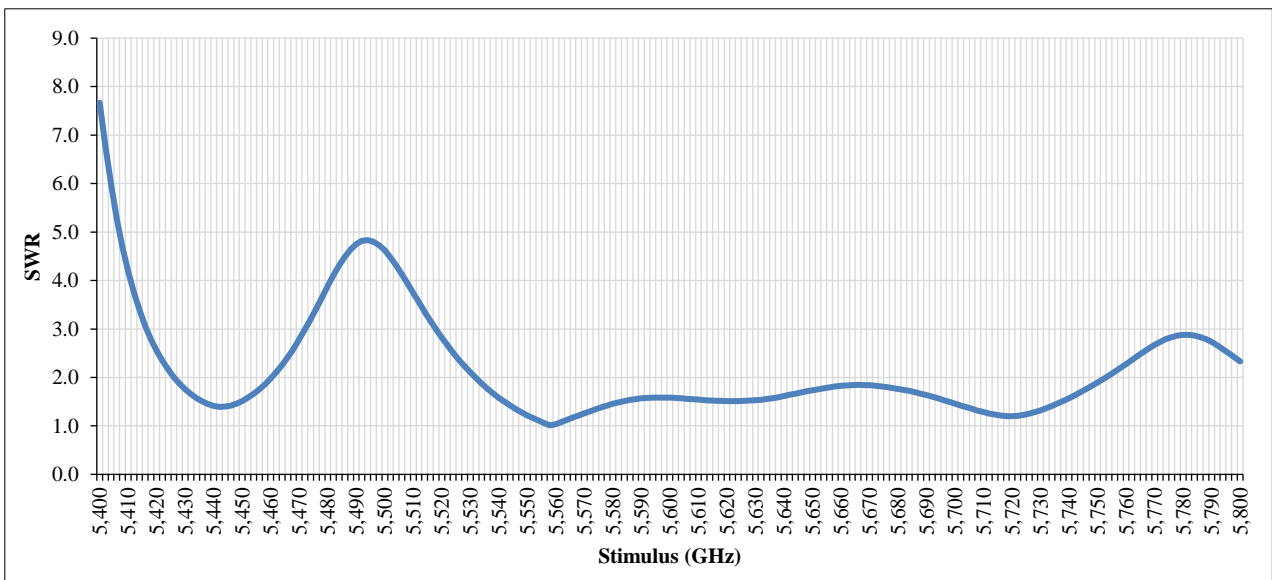


Figure 7. SWR measurement of the lower antenna with the corrugation plate

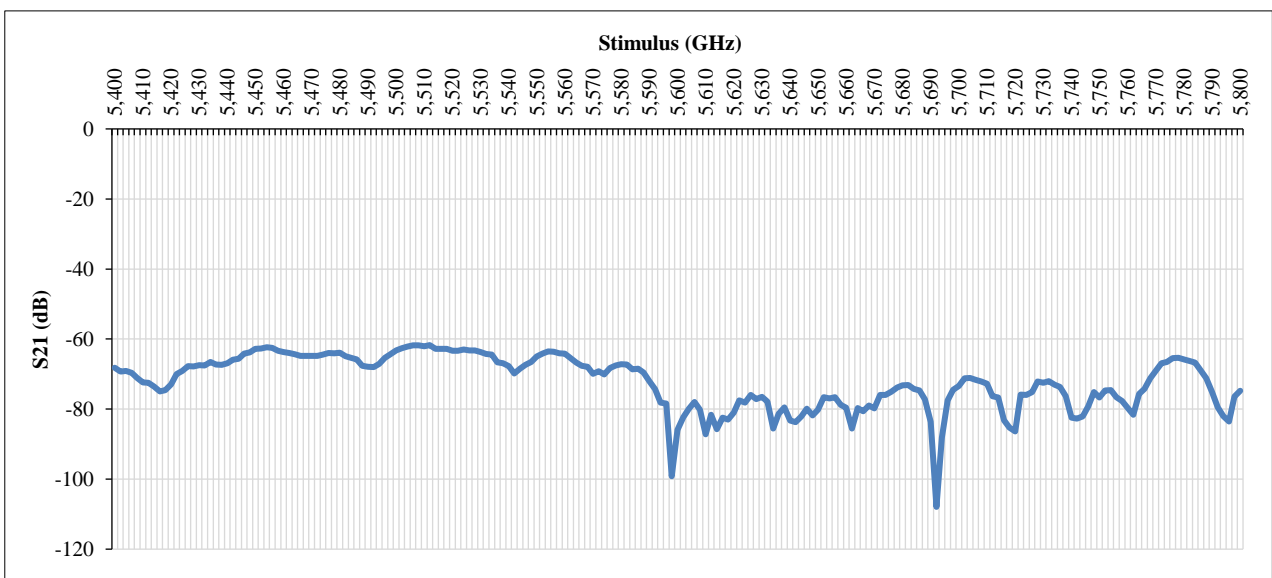


Figure 8. S21 measurement of the upper antenna with the corrugation plate

The S12 reduction with the plate (Figures 8 and 9) can be explained by a redistribution of the surface/fringing fields that weakens unintended coupling paths between ports. Conceptually, the plate imposes a modified boundary condition acting like a weak parasitic/superstrate: it attenuates leakage that would otherwise flow along the structure and radiate back toward Port 1. Similar isolation improvements are reported when parasitic layers, EBG/FSS loading for defected grounds, are introduced in compact arrays to suppress mutual coupling.

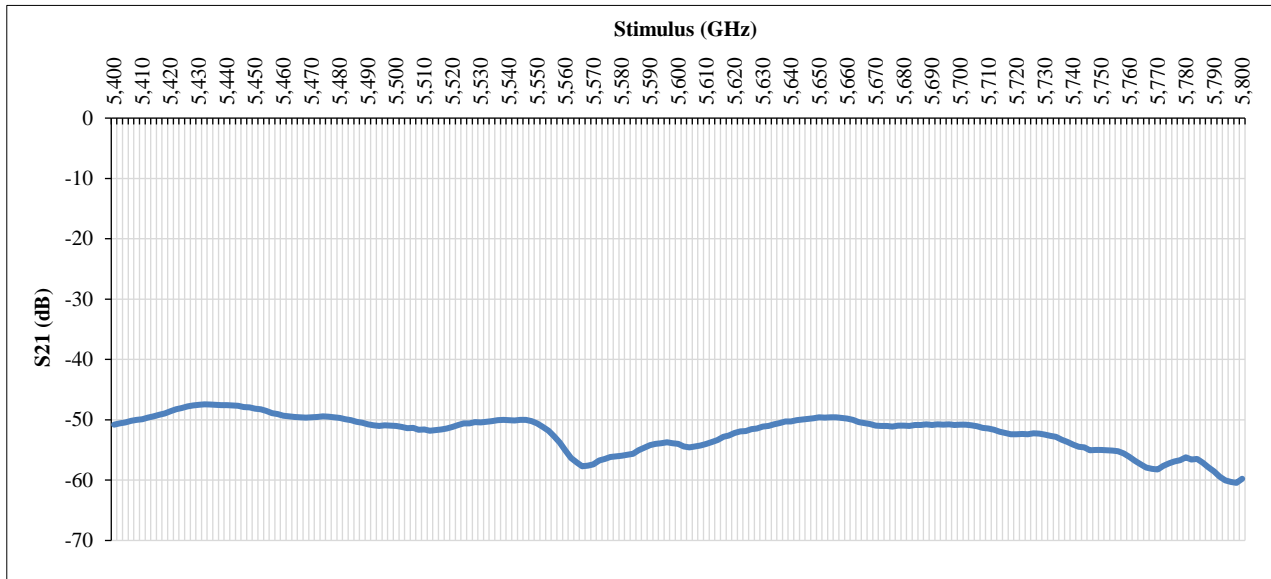


Figure 9. S21 measurement of the lower antenna without the corrugation plate

Minor frequency shifts (kHz-MHz scale) between simulation and measurement are expected at C-band and can arise from small deviations in effective permittivity, conductor thickness, solder pad geometry, and plate height. Because the resonant frequency scales with both the effective electrical length of the patch and the total dielectric environment, small fabrication/assembly drifts naturally move the return-loss dip and SWR minimum slightly from their simulated locations. In this prototype, we did not measure radiation patterns /HPBW. HPBW values are simulation results only.

Complementing this, the S11 measurement using the corrugation plate (Figure 4) clearly exhibited a strong resonance at approximately 5.6 GHz, with both the upper-antenna (blue trace) and lower-antenna (purple trace) displaying deep return-loss minima—indicative of strong matching performance in the assembled configuration. When examining the isolated upper antenna with the corrugation plate (Figure 4), the S11 dip remains pronounced at this resonance frequency, confirming that the plate contributes effectively to impedance tuning. Conversely, the lower antenna measured without the corrugation plate (Figure 4) shows a shallower return-loss notch around 5.6 GHz, underscoring the plate's role in enhancing resonance depth and overall matching quality.

Taken together, these S11 curves confirm that the corrugation plate substantially improves return loss—reducing impedance mismatch and boosting antenna performance at the intended operational frequency. This experimental outcome supports the overall design, evidencing that the antenna system, with the plate in place, achieves superior matching as expected from simulations.

The measurement phase of this study revealed notable challenges concerning beamwidth specifications. The results indicate that the horizontal beamwidth was measured at approximately 8 degrees, which is slightly above the simulated value of 7.1 degrees. More strikingly, the vertical beamwidth measurement approached 30 degrees—considerably wider than the simulated 17.4 degrees and significantly exceeding the desired maximum specification of 7.5 degrees [16]. These discrepancies raise important concerns regarding the accurate translation of simulated antenna designs into tangible prototypes. They highlight the need for further targeted refinements in the design and manufacturing processes. Key areas for improvement include enhancing manufacturing precision, ensuring proper alignment of antenna elements, and exercising stringent control over environmental conditions during the measurement processes. Such refinements are critical for bridging the gap between simulated models and physical realizations of antenna systems.

In addition of S11 data, the S21 measurements further illustrate the influence of the corrugation plate on signal behavior. The upper antenna measured with the corrugation plate (Figure 8) shows a pronounced dip at ~5.6 GHz, indicating a strong transmission characteristic tuned precisely to the operational frequency. In contrast, the lower antenna measured without the corrugation plate (Figure 9) exhibits a considerably flatter and less pronounced response, reflecting reduced transmission efficiency and weaker coupling at the same frequency.

These S21 curves underscore the plate's essential role in enhancing forward signal transmission. When combined with the earlier S11 results, the data collectively confirm that the corrugation plate significantly improves both

impedance matching and inter-port coupling. This behavior is consistent with expectations for well-matched two-port networks and supports the design objective of optimized radar performance as discussed in Section 3.3.3.

The measurement phase also revealed notable challenges concerning beamwidth specifications. The results indicate that the horizontal beamwidth was measured at approximately 8° , slightly above the simulated value of 7.1° . More strikingly, the vertical beamwidth measurement approached 30° , which are considerably wider than the simulated 17.4° and significantly exceeding the desired maximum specification of 7.5° [16]. These discrepancies raise important concerns regarding accurate translation of simulated antenna designs into tangible prototypes. They highlight the need for further targeted refinements in the design and manufacturing processes. Key areas for improvement include enhancing manufacturing precision, ensuring proper alignment of antenna elements, and exercising stringent control over environmental conditions during the measurement processes. Such refinements are critical for bridging the gap between simulated models and physical realizations of antenna systems.

Further insight is provided by the SWR measurements for both antennas, presented in Figures 5 to 7 and 10. These plots measure the SWR (Standing Wave Ratio). Figure 5 – SWR of the upper antenna with the corrugation plate: A pronounced trough appears near the operational frequency (~ 5.6 GHz), with SWR dipping close to 1.2–1.3:1. This highlight very good match and minimal reflection at resonance. Figure 6 – SWR of the upper antenna without the plate: The trough is noticeably broader and shallower, centering slightly off-frequency, with SWR values rising above 1.5:1 around 5.6 GHz. This indicates reduced impedance matching and a less efficient coupling. Figure 7 – SWR of the lower antenna with the corrugation plate : Similar to graph (a), a well-defined dip near 5.6 GHz demonstrates that the plate effectively enhances matching for the lower element as well. Figure 10 – SWR of the lower antenna without the plate: Exhibits a flattened response with elevated SWR, often above 1.5, signifying poorer matching and increased reflected power.

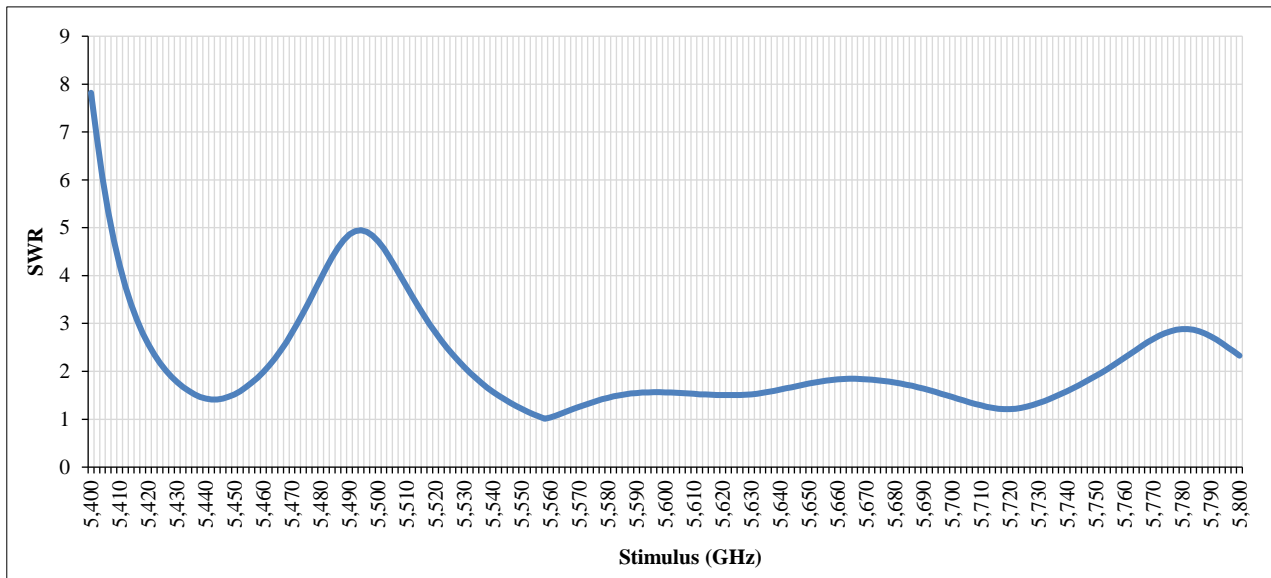


Figure 10. SWR measurement of the lower antenna without the corrugation plate

These results underscore the plate's critical role in tuning: it not only deepens the SWR minimum—bringing it closer to the ideal 1:1—but also sharpens the resonance, concentrating good match behavior directly at the intended frequency band. In contrast, removing the plate causes mismatch, broader resonance, and more power reflection—consistent with standard SWR theory.

Notably, the combined S_{11} , S_{21} , and SWR data consistently verify that: (i) With the corrugation plate installed, both antenna elements exhibit optimal matching ($\text{SWR} \approx 1.2\text{--}1.3$) precisely at 5.6 GHz, suggesting efficient power transfer and minimal return loss. (ii) Without the plate, matching degrades, and resonance becomes less confirming the plate's tuning necessity. Together, these SWR findings support the earlier assertions regarding improved impedance matching and signal coupling due to the corrugation plate. They reinforce the conclusion that the design modifications successfully translate simulated impedance characteristics into physical prototype behavior.

6- Extended Measurement and Analysis

To further validate the antenna's performance and assess the influence of structural modifications, an extended analysis was conducted comparing the measured S-parameters against the simulated results for both configurations—with and without the corrugation plate. As shown in Figure 11, the configuration with the corrugation plate demonstrates strong agreement between simulation and measurement across the full frequency span of 5.40–5.80 GHz. In particular,

the S11 parameter exhibits a deep resonance at ~ 5.6 GHz, with the measured return loss closely tracking the simulated dip. Similarly, the S21 transmission characteristics also show consistent behavior between the modeled and experimental data, indicating effective signal coupling and minimal mismatch.

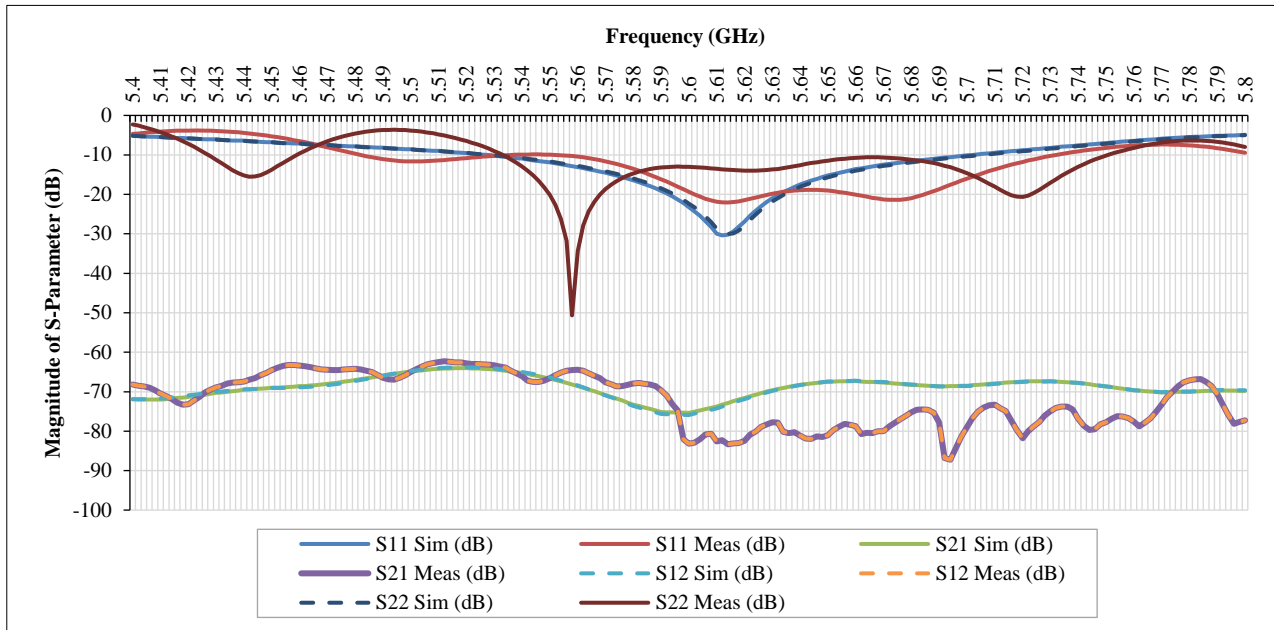


Figure 11. Comparison between simulation and measurement results with the corrugation plate

In contrast, Figure 12, which presents the performance without the corrugation plate, reveals larger deviations between simulated and measured results. The S11 and S21 curves both exhibit reduced depth and slight frequency shifts in the resonance point, signalling degraded impedance matching and reduced transmission efficiency. Notably, the S12 parameter—which represents reverse isolation—undergoes a significant change compared to the configuration with the plate, with the measured S12 curve showing higher and more fluctuating values, indicating increased mutual coupling or signal leakage between ports. This suggests that the corrugation plate plays a critical role in suppressing backward coupling and improving isolation performance. In contrast, the S22 parameter, both in simulation and measurement, remains relatively consistent across both configurations, with only minimal variation. This stability suggests that the antenna's input match at port 2 is less sensitive to the presence of the plate and is likely more robust to structural changes.

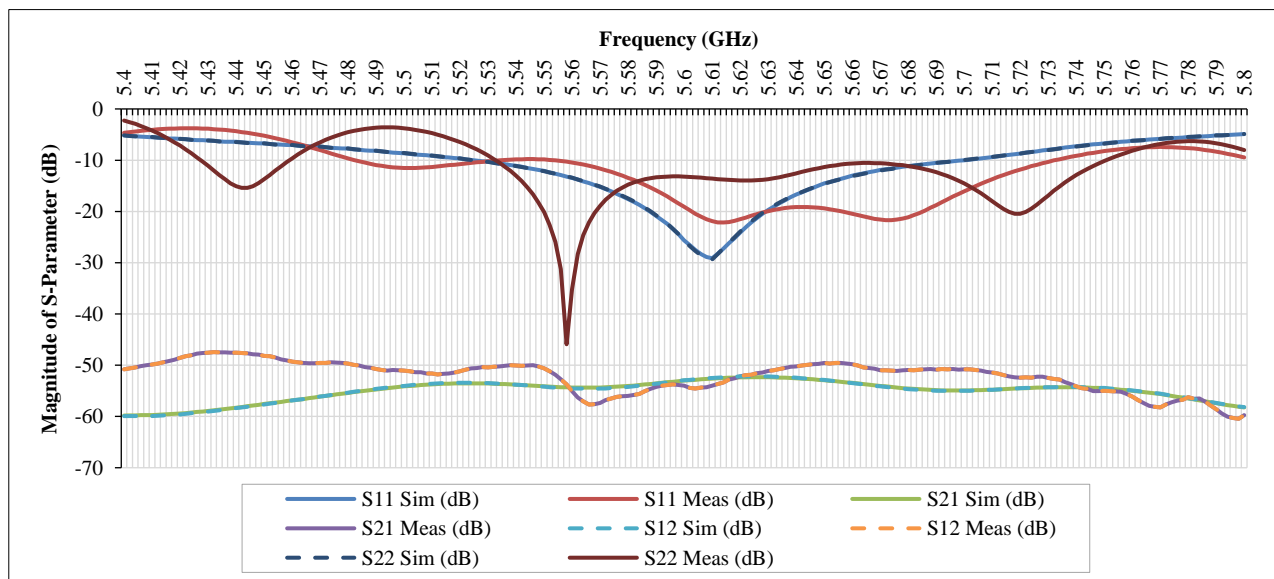


Figure 12. Comparison between simulation and measurement results without the corrugation plate

The overlays in Figure 11 (with plate) show strong simulation-measurement congruence on S11 and S21, implying that the dominant EM behaviors are well captured by the model once the plate's reactive loading is included. In Figure 11 (without plate), shallower S11 minima and flatter S21 are consistent with higher mismatch loss and weaker forward coupling. The higher and more variable S12 further indicates that back-coupling paths are less controlled. This

asymmetry underscores the plate's role as a lightweight, fabrication-friendly tuning feature that stabilizes both matching and isolation and thereby improves simulation measurement correlation. Pattern-level validation (HPBW, sidelobes) was not conducted in this prototype. The remaining simulation-only HPBW gaps align with sensitives summarized in section 3.34. With the plate, the prototype achieves the intended matching/transmission/isolation improvements and a closer simulation-measurement agreement for S-parameters.

To contextualize the present prototype, Table 1 compares key measured metrics (S-parameters, SWR < gain) against our earlier works, while explicitly separating HPBW as simulation-only. The table highlights how the current prototype (with and without the corrugation plate) progresses on matching and transmission. It also clarifies that beamwidth remains a simulation-only gap for this build. Relative to the 2021 prototype, the corrugation plate deepens the return-loss minimum and improves SWR (≈ 1.2 - 1.3), consistent with the input-admittance tuning in section 3.3.3. Concurrent S21 and S12 indicate better forward power transfer and weaker reverse coupling. The simulated HPBW values remain wider than the $2.8^\circ/7.5^\circ$ targets, consistent with aperture limits, and coupling/edge effects summarized in sections 3.3.4. The plate helps center the match near the design frequency and stabilizes the two-port behavior, which is marked by the relatively unchanged S22. Against our earlier work, the current prototype improves matching, transmission, and isolation while preserving gain. HPBW remains a simulation-only gap for this prototype, motivating next-step pattern-control (e.g., mild taper, EBG/FSS/superstrate) and alignment-controlled pattern measurements.

Table 1. Comparison of the present work with our previous studies

Parameters	Study/Configuration				
	Measurement with corrugation plate	Measurement without corrugation plate	Simulation (4×12)	Simulation (4×12) [15]	Measurement (4×12) [16]
Return Loss S11 (db)	≈ -27.35	≈ -27.35 (shallower notch)	-	≈ -30	≈ -27.35 (minimum at ~ 5.64 GHz)
SWR	≈ 1.2 - 1.3	> 1.5	-	-	-
Gain (dBi)	> 20	> 20	-	21.66	> 20
HPBW (Azimuth, in degrees)	≈ 8	≈ 8	$\approx 7.1^\circ$	7.1	≈ 8
HPBW (Elevation, in degree)	- (not measured)	- (not measured)	$\approx 17.4^\circ$	17.4°	≈ 8
Polarization	Horizontal	Horizontal	Horizontal	Horizontal	Horizontal

7- Conclusions

This study successfully demonstrated the design, simulation, and experimental validation of a high-gain antenna system operating at approximately 5.6 GHz, with an emphasis on the role and influence of the corrugation plate. Across a range of measurements—including S-parameters (S11, S21, S12, S22), SWR, and beamwidth analysis—the fabricated prototype exhibited strong alignment with simulated predictions, affirming the antenna's suitability for radar applications. The return loss (S11) measurements reached values near -27.35 dB, confirming effective impedance matching, while the antenna gain exceeded the 20 dBi threshold, meeting critical performance targets.

The presence of the corrugation plate significantly enhanced the antenna's performance by improving impedance matching, reducing SWR to values near 1.2–1.3, and increasing transmission efficiency (S21). Without the plate, measurements revealed degraded matching, broader resonances, and higher SWR, reinforcing the plate's importance in achieving well-tuned and narrowband behavior. Additionally, an extended comparison between simulation and measurement—both with and without the corrugation plate—highlighted the plate's impact on improving agreement between modeled and real-world data. The S12 parameter, representing reverse isolation, was found to be notably affected by the absence of the plate, indicating greater inter-port coupling. Meanwhile, S22 remained relatively stable, showing little variation regardless of configuration.

Despite these successes, challenges remain—particularly regarding beamwidth performance. The measured vertical beamwidth exceeded both the simulated value and design specification by a significant margin (30° measured vs. 17.4° simulated), suggesting limitations in the physical realization of the simulated design. These results underscore the need for further refinement in the manufacturing process, mechanical alignment, and environmental control during testing.

To further enhance the antenna system's performance and address the noted discrepancies, several future research directions are recommended. First, refinement of the antenna fabrication process is essential to minimize dimensional variances that contribute to mismatch and beam distortion. In particular, improving the mechanical precision and alignment of the corrugation plate and antenna elements could yield better control over beamwidth characteristics, especially in the vertical plane. Additionally, investigating alternative matching structures or tuning elements may help achieve narrower beamwidths without compromising impedance performance. A more robust environmental control setup during measurements is also advised to isolate the impact of external factors. Further parametric studies using simulation tools should be conducted to explore the sensitivity of design parameters on real-world performance, allowing for iterative improvements before physical prototyping. Finally, fabrication and measurement robustness evaluation should be included in future plans: fabricate three or more units to capture build variance; introduce alignment jigs and a documented calibration/uncertainty budget (repeat OSL/TRL, fixture de-embedding); and re-measure radiation patterns with alignment verification to reduce elevation-cut inflation.

8- Declarations

8-1-Author Contributions

Conceptualization, I.J.M.E.; methodology, I.J.M.E. and D.D.; software, A.M.; validation, I.J.M.E., E.B., and W.S.; formal analysis, T.H. and E.B.; investigation, D.F.H.; resources, I.J.M.E., A.M., and D.F.H.; data curation, E.B. and I.J.M.E.; writing—original draft preparation, I.J.M.E., A.M., T.H., and W.S.; writing—review and editing, I.J.M.E., W.S., and Y.A.H.; visualization, S.A.N., A.M., and E.B.; supervision, I.J.M.E. and D.F.H.; project administration, K. and N.A.R.; funding acquisition, K. and N.A.R. All authors have read and agreed to the published version of the manuscript.

8-2-Data Availability Statement

The data presented in this study are available on request from the corresponding author.

8-3-Funding

This research was funded by the Lembaga Pengelola Dana Pendidikan (LPDP), Ministry of Finance of the Republic of Indonesia.

8-4-Acknowledgements

The authors would like to thank the Lembaga Pengelola Dana Pendidikan (LPDP), Ministry of Finance of the Republic of Indonesia, for funding this research. The authors also express their appreciation to Institut Teknologi Bandung, Universitas Pendidikan Indonesia, Universitas Sangga Buana, and PT Kirei for their support and collaboration throughout the project. Special thanks go to the technical and administrative teams who contributed during the design, fabrication, and evaluation of the C-band microstrip antenna array.

8-5-Institutional Review Board Statement

Not applicable.

8-6-Informed Consent Statement

Not applicable.

8-7-Conflicts of Interest

The authors declare that there is no conflict of interest regarding the publication of this manuscript. In addition, the ethical issues, including plagiarism, informed consent, misconduct, data fabrication and/or falsification, double publication and/or submission, and redundancies have been completely observed by the authors.

9- References

- [1] Davis, M. E. (2015). A history of battlefield surveillance radar. 2015 IEEE Radar Conference (RadarCon), 1345–1350. doi:10.1109/radar.2015.7131204.
- [2] Heinbach, K., Painter, R., & Pace, P. (2014). Commercially available low probability of intercept radars and non-cooperative ELINT receiver capabilities. Naval Postgraduate School, Center for Joint Services Electronic Warfare, Monterey, United States.
- [3] Park, J., Park, S., Kim, D. H., & Park, S. O. (2019). Leakage mitigation in heterodyne FMCW radar for small drone detection with stationary point concentration technique. IEEE Transactions on Microwave Theory and Techniques, 67(3), 1221–1232. doi:10.1109/TMTT.2018.2889045.
- [4] GmbH. (2025). SQUIRE Ground Surveillance Radar. Thales Electronic Systems GmbH, Ditzingen, Germany.
- [5] Sayed, A. N., Ramahi, O. M., & Shaker, G. (2024). Frequency-Modulated Continuous-Wave Radar Perspectives on Unmanned Aerial Vehicle Detection and Classification: A Primer for Researchers with Comprehensive Machine Learning Review and Emphasis on Full-Wave Electromagnetic Computer-Aided Design Tools. Drones, 8(8), 370. doi:10.3390/drones8080370.
- [6] Liu, B. (2024). PLL Designs for FMCW Radar Systems. PhD Thesis, University of California, Berkeley, United States.
- [7] Apriono, C., Mahatmanto, B. P. A., & Juwono, F. H. (2023). Rectangular Microstrip Array Feed Antenna for C-Band Satellite Communications: Preliminary Results. Remote Sensing, 15(4), 1126. doi:10.3390/rs15041126.
- [8] Ruliyanta, R., Nugroho, R., & Asyifa, D. (2024). Design of Rectangular Patch Array 2x4 Microstrip Antenna on C-Band for Weather Radar Applications. Journal of Telecommunication, Electronic and Computer Engineering (JTEC), 16(1), 7–11. doi:10.54554/jtec.2024.16.01.002.
- [9] Nabi, R., Wei-Jun, L., & Majeed, M. R. (2024). Design of Microstrip Array Antenna for Vehicle Millimeter Wave Radar. European Journal of Electrical Engineering and Computer Science, 8(2), 77–90. doi:10.24018/ejece.2024.8.2.611.

- [10] Phakaew, T., Pongthavornkamol, T., Torrungrueng, D., Dallmann, T., & Chalermwisutkul, S. (2025). A Wideband 4×4 Patch Array Antenna With Low Sidelobes for Radar-Based Obstacle Detection in Railway Transportation. *IEEE Open Journal of Antennas and Propagation*, 6(3), 774–788. doi:10.1109/OJAP.2025.3548112.
- [11] Saeed, M. A., & Nwajana, A. O. (2023). A review of beamforming microstrip patch antenna array for future 5G/6G networks. *Frontiers in Mechanical Engineering*, 9. doi:10.3389/fmech.2023.1288171.
- [12] Alshrafi, W. (2022). Grating lobe suppression in microstrip patch uniform linear array antennas using passive structures. Ph.D. Thesis, RWTH Aachen University, Aachen, Germany.
- [13] Puklibmoung, T., & Sa-Ngiamvibool, W. (2022). Design and Fabrication of Broad-Beam Microstrip Antenna Using Parasitic Patches and Cavity-Backed Slot Coupling. *Applied System Innovation*, 5(2), 31. doi:10.3390/asi5020031.
- [14] Bhattacharjee, S., Mandal, S., Ghosh, C. K., & Banerjee, S. (2022). Reduction of Mutual Coupling and Cross-Polarization of Microstrip MIMO Antenna Using Electromagnetic Soft Surface (EMSS). *Radio Science*, 57(5), 1-10. doi:10.1029/2021RS007377.
- [15] Shalannanda, W., & Hariyadi, T. (2019). Design and Simulation of C-Band Antenna for Portable Ground Surveillance Radar. *Proceeding of 2019 5th International Conference on Wireless and Telematics, ICWT 2019*, 1–4. doi:10.1109/ICWT47785.2019.8978234.
- [16] Shalannanda, W., & Hariyadi, T. (2019). Design and Simulation of C-Band Antenna for Portable Ground Surveillance Radar. *2019 IEEE 5th International Conference on Wireless and Telematics (ICWT)*, 1–4. doi:10.1109/icwt47785.2019.8978234.
- [17] Chen, Q., Yan, S., Guo, X., Wang, W., Huang, Z., Yang, L., Li, Y., & Liang, X. (2023). A low sidelobe 77 GHz centre-fed microstrip patch array antenna. *IET Microwaves, Antennas and Propagation*, 17(11), 887–896. doi:10.1049/mia2.12408.
- [18] Swapna, S., Karthikeya, G. S., Koul, S. K., & Basu, A. (2024). A High Gain Multi-Port Series Fed Array Realized with Micromachined Low-Cost 3D-Printed Substrate. *IETE Technical Review (Institution of Electronics and Telecommunication Engineers, India)*, 41(3), 287–296. doi:10.1080/02564602.2023.2242828.
- [19] Ashfaq, M., Bashir, S., Hussain Shah, S. I., Abbasi, N. A., Rmili, H., & Khan, M. A. (2022). 5G Antenna Gain Enhancement Using a Novel Metasurface. *Computers, Materials and Continua*, 72(2), 3601–3611. doi:10.32604/cmc.2022.025558.
- [20] Wang, H., Huang, X. B., & Fang, D. G. (2008). A single layer wideband U-slot microstrip patch antenna array. *IEEE Antennas and Wireless Propagation Letters*, 7, 9–12. doi:10.1109/LAWP.2007.914122.
- [21] Huque, M. T. I. U., Hosain, M. K., Islam, M. S., & Chowdhury, M. A. A. (2011). Design and performance analysis of microstrip array antennas with optimum parameters for X-band applications. *International journal of advanced computer science and applications*, 2(4), 81-87. doi:10.14569/ijacsa.2011.020413.
- [22] Mandal, S., & Ghosh, C. K. (2022). Mutual Coupling Reduction in a Patch Antenna Array Based on Planar Frequency Selective Surface Structure. *Radio Science*, 57(2), 1-11. doi:10.1029/2021RS007392.
- [23] Alsudani, A., & Marhoon, H. M. (2023). Design and Enhancement of Microstrip Patch Antenna Utilizing Mushroom Like-EBG for 5G Communications. *Journal of Communications*, 18(3), 156–163. doi:10.12720/jcm.18.3.156-163.
- [24] Yalcinkaya, M. T., Kamal, S., Sen, P., & Fettweis, G. P. (2024). The Causal Nexus Between Different Feed Networks and Defected Ground Structures in Multi-Port MIMO Antennas. *Sensors*, 24(22), 7278. doi:10.3390/s24227278.
- [25] Tunio, I. A., Mahe, Y., Razban-Haghighi, T., & Froppier, B. (2021). Mutual Coupling Reduction in Patch Antenna Array Using Combination of Shorting Pins and Metallic Walls. *Progress In Electromagnetics Research C*, 107, 157–171. doi:10.2528/pierc20082803.
- [26] Zhu, J., & Liu, J. (2025). Design of Microstrip Antenna Integrating 24 GHz and 77 GHz Compact High-Gain Arrays. *Sensors*, 25(2), 481. doi:10.3390/s25020481.